Molecular Cell, Volume *75*

Supplemental Information

Structural Basis of BRCC36 Function in DNA Repair and Immune Regulation

Julius Rabl, Richard D. Bunker, Andreas D. Schenk, Simone Cavadini, Mark E. Gill, Wassim Abdulrahman, Amparo Andrés-Pons, Martijn S. Luijsterburg, Adel F.M. Ibrahim, Emma Branigan, Jacob D. Aguirre, Aimee H. Marceau, Claire Guérillon, Tewis Bouwmeester, Ulrich Hassiepen, Antoine H.F.M. Peters, Martin Renatus, Laurent Gelman, Seth M. Rubin, Niels Mailand, Haico van Attikum, Ronald T. Hay, and Nicolas H. Thomä

A

protein	alternative names	entrez	length	Da
ABRAXAS	ABRA1, ABRX1, CCDC98, FAM175A	84142	409	46663
ABRO1	ABRX2, KIAA0157, FAM175B	23172	415	46901
BRCA1	BRCAI, BRCC1, BROVCA1, IRIS, FANCS, PNCA4, PPP1R53, PSCP, RNF53	672	1863	207721
BRCC36	BRCC3, C6.1A, CXorf53	79184	316	36072
BRE	BABAM2, BRCC4, BRCC45	9577	383	43552
MERIT40	BABAM1, C19orf62, HSPC142, NBA1	29086	329	36560
RAP80	UIMC1, RXRIP110, X2HRIP110	51720	719	79727
SHMT2	GLY A+, GLYA, GLYM, HEL-S-51e	6472	504	55993

B

```
SP|Q6UWZ7|ABRX1_HUMAN MEGESTSAVLSGFVLGALAFQHLNTDSDTEGFLLGEVKGEAKNSITDSQMDDVEVVYTID 60
SP|Q15018|ABRX2_HUMAN -----MAASISGYTFSAVCFHSANSNADHEGFLLGEVRQEETFSISDSQISNTEFLQVIE 55
                        :* :**:.:.*:.*:  *:::* ********: * . **:***:.:.*.: .*:

SP|Q6UWZ7|ABRX1_HUMAN IQKYIPCYQLFSFYNSSGEVNEQALKKILSNVKKNVVGWYKFRRHSDQIMTFRERLLHKN 120
SP|Q15018|ABRX2_HUMAN IHNHQPCSKLFSFYDYASKVNEESLDRILKDRRKKVIGWYRFRRNTQQQMSYREQVLHKQ 115
                        *::: ** :*****: :.:***::*.:**.: :*:*:***:******:* *::**::***:

SP|Q6UWZ7|ABRX1_HUMAN LQEHFSNQDLVFLLLTPSIITESCSTHRLEHSLYKPQKGLFHRVPLVVANLGMSEQLGYK 180
SP|Q15018|ABRX2_HUMAN LTRILGVPDLVFLLFS-FISTANNSTHALEYVLFRPNRRYNQRISLAIPNLGNTSQQEYK 174
                        * . :.  ******::  * * . *** **: *::*::   :*: *.: *** :.*  **

SP|Q6UWZ7|ABRX1_HUMAN TVSGSCMSTGFSRAVQTHSSKFFEEDGSLKEVHKINEMYASLQEELKSICKKVEDSEQAV 240
SP|Q15018|ABRX2_HUMAN VSSVPNTSQSYAKVIKEHGTDFFDKDGVMKDIRAIYQVYNALQEKVQAVCADVEKSERVV 234
                        . *    * .:::.:: *.:.**::** :*::: * ::* :***::::* .**.**:.*

SP|Q6UWZ7|ABRX1_HUMAN DKLVKDVNRLKREIEKRRGAQIQAAREKNIQKDP-QENIFLCQALRTFFPNSEFLHSCVM 299
SP|Q15018|ABRX2_HUMAN ESCQAEVNKLRRQITQRKNEKEQERRLQQAVLSRQMPSESLDPAFSPRMPSSGFAAEGRS 294
                        :.   :**:*:*:* :*:. : *  * ::   .    .  *  *:   :*.* *  .

SP|Q6UWZ7|ABRX1_HUMAN SLKNRHVSKSSCNYNHHLDVVDNLTLMVEHTDIPEASPASTPQIIKHKALD-LDDRWQFK 358
SP|Q15018|ABRX2_HUMAN TLGDAEASDPPPPYSDFHPNNQES--TLSHSRMERSVFMPRPQAVGSSNYASTSAGLKYP 352
                        :* : ..*.    *...    ::    :.*: : .:     ** :  .     .   ::

SP|Q6UWZ7|ABRX1_HUMAN RSRLLDTQDKRSKADTGSSNQD--------------------KASKMSSPETDEEIEKM 397
SP|Q15018|ABRX2_HUMAN GSGADLPPPQRAAGDSGEDSDDSDYENLIDPTEPSNSEYSHSKDSRPMAHPDEDPRNTQT 412
                         *       :*: .*:*...:*                    .:  *: *: * .  :

SP|Q6UWZ7|ABRX1_HUMAN KGFGEYSRSPTF 409
SP|Q15018|ABRX2_HUMAN SQI--------- 415
                        . :
```

C

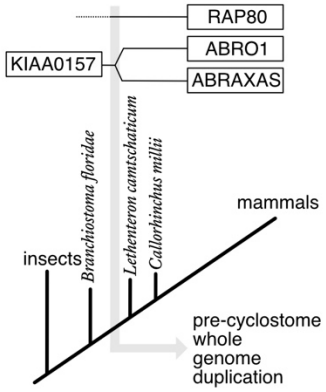

D

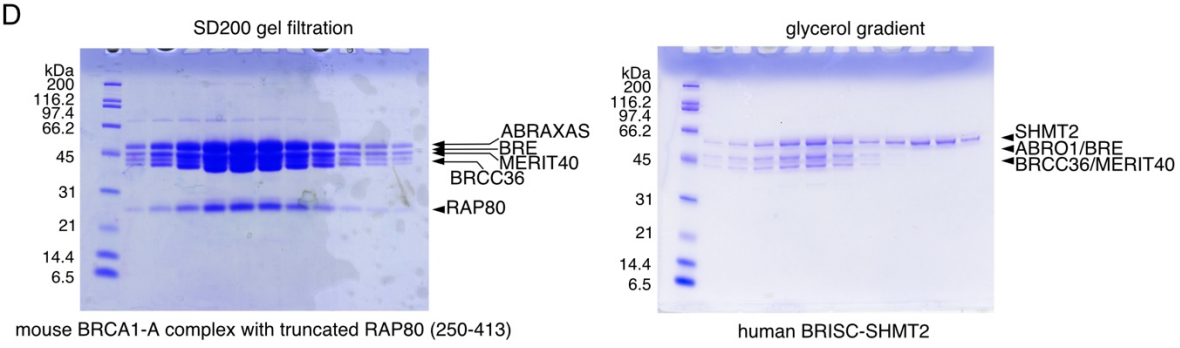

mouse BRCA1-A complex with truncated RAP80 (250-413)

human BRISC-SHMT2

Figure S1. Overview of protein subunits of the BRCA1-A and BRISC complexes, Related to Figure 1

(A) Protein subunits of BRCA1-A and BRISC.

(B) Protein sequence alignment of human ABRAXAS and ABRO1.

(C) Schematic representation of the evolutionary origin of ABRAXAS and ABRO1. Up to and including the lancelet *Branchiostoma floridae* (GCA_000003815.1) animals contain only a single ancestral precursor to ABRAXAS and ABRO1, KIAA0157, and no RAP80. The arctic lamprey *Lethenteron camtschaticum* (GCA_000466285.1) and elephant shark *Callorhinchus milii* (GCA_000165045.2) genomes already contain the two homologs, ABRAXAS and ABRO1, and RAP80, suggesting that they arose during the whole genome duplication preceding the development of cyclostomes (Putnam et al., 2008).

(D) SDS-PAGE analysis of mouse BRCA1-A complex size exclusion chromatography fractions used for crystallization and of human BRISC-SHMT2α complex glycerol gradient fractions (higher to lower density) used for cryo-EM structure determination.

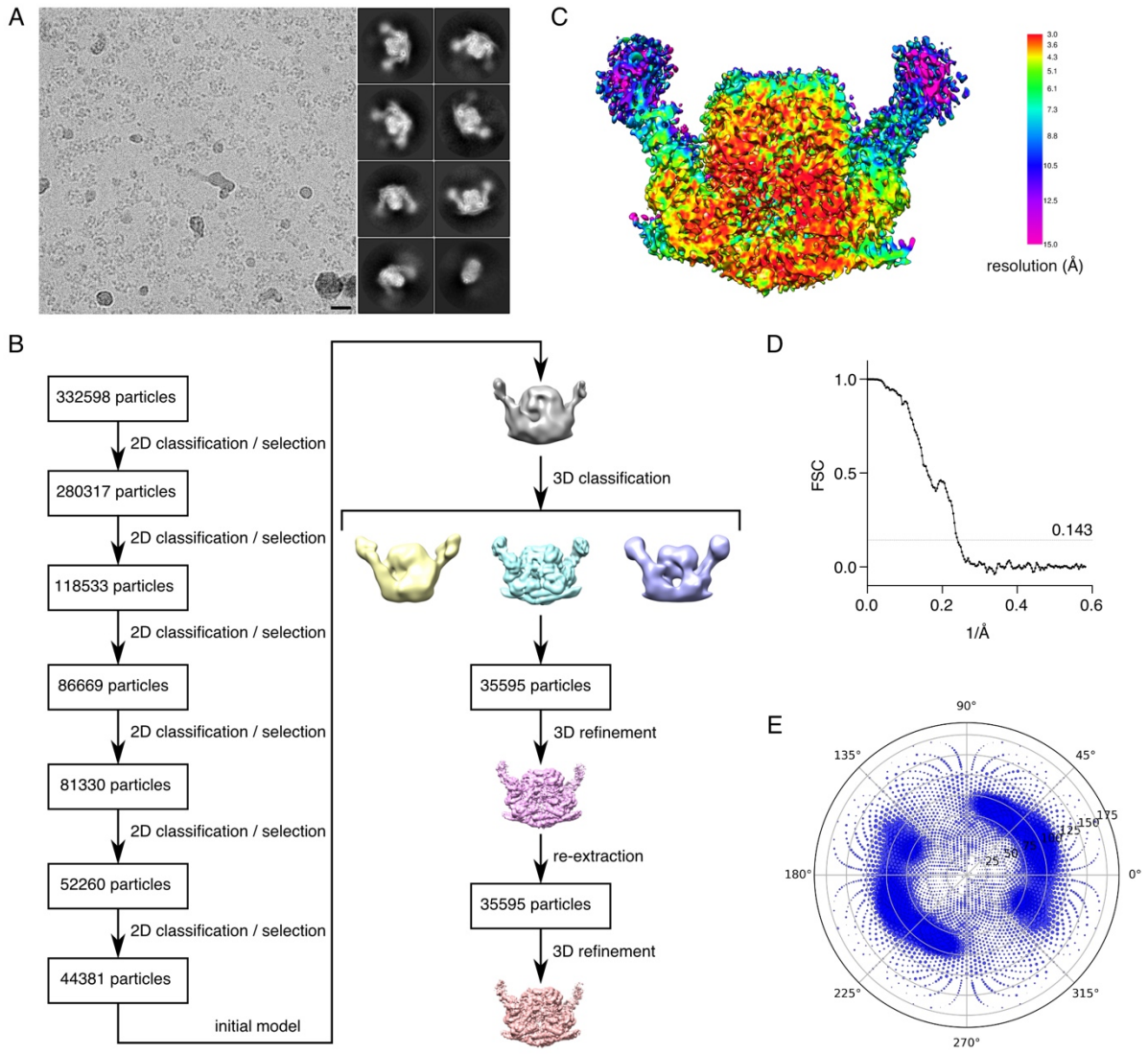

Figure S2. Cryo-EM classification and refinement procedures for BRISC-SHMT2α complex, Related to Figure 1

(A) Representative micrograph (scale bar: 300 Å) and reference-free class averages.

(B) Flowchart representation of data processing strategy.

(D) Gold-standard Fourier shell correlation (FSC) curve.

(E) Angular distribution of particles.

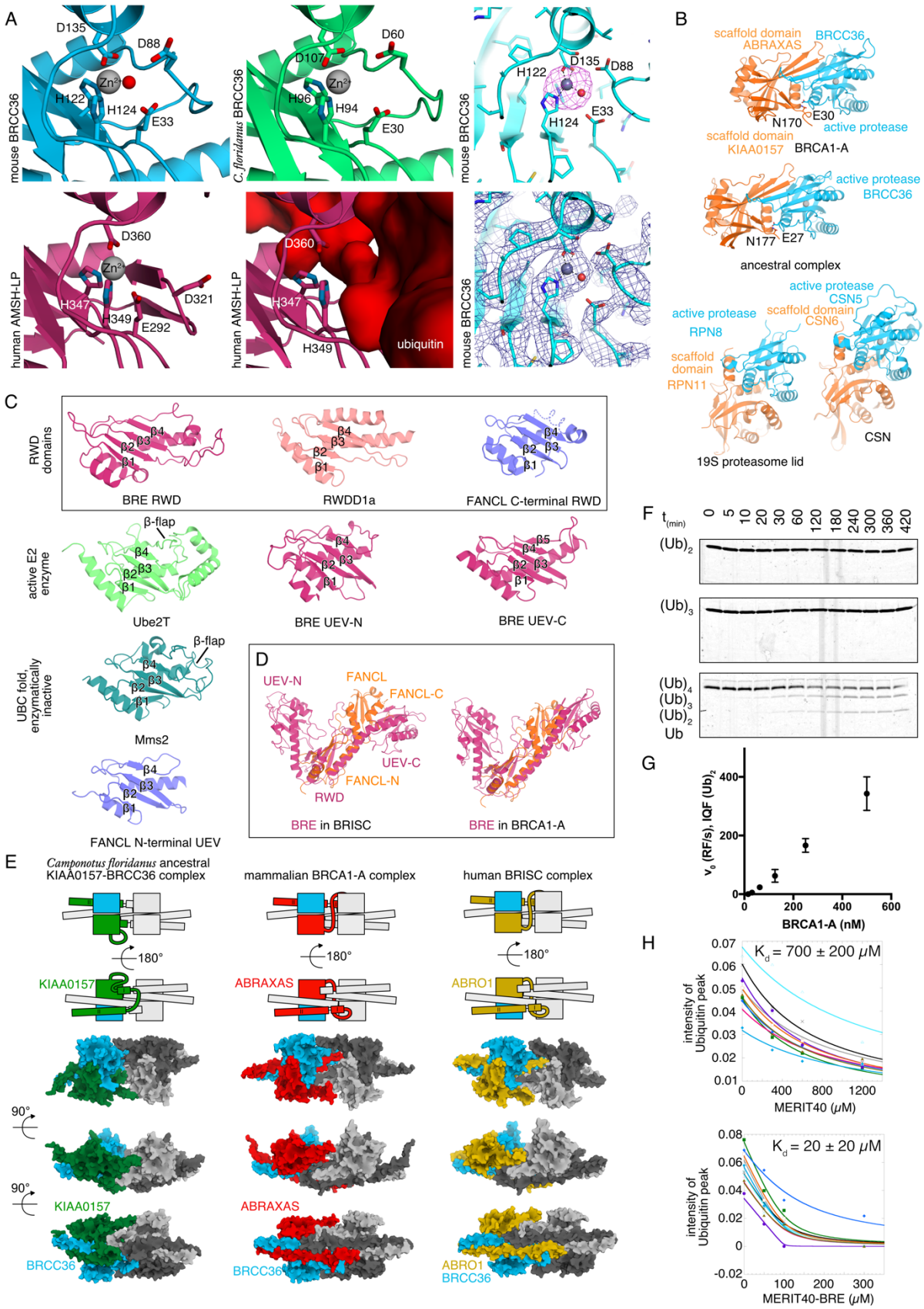
A
mouse BRCC36
D135
D88
H122
H124
E33
C. floridanus BRCC36
D60
D107
H96
H94
E30
mouse BRCC36
H122
D135
D88
H124
E33
human AMSH-LP
D360
H347
H349
E292
D321
human AMSH-LP
D360
H347
H349
ubiquitin
mouse BRCC36
B
scaffold domain
ABRAXAS
BRCC36
N170
E30
active protease
scaffold domain
KIAA0157
BRCA1-A
active protease
BRCC36
N177
E27
ancestral complex
active protease
CSN5
active protease
scaffold domain
CSN6
RPN8
scaffold
domain
RPN11
CSN
19S proteasome lid
C
RWD domains
β1
β2
β3
β4
BRE RWD
RWDD1a
FANCL C-terminal RWD
active E2 enzyme
β-flap
Ube2T
BRE UEV-N
β5
BRE UEV-C
UBC fold, enzymatically inactive
Mms2
FANCL N-terminal UEV
D
UEV-N
FANCL
FANCL-C
UEV-C
FANCL-N
RWD
BRE in BRISC
BRE in BRCA1-A
E
Camponotus floridanus ancestral KIAA0157-BRCC36 complex
mammalian BRCA1-A complex
human BRISC complex
180°
KIAA0157
ABRAXAS
ABRO1
90°
90°
KIAA0157
BRCC36
ABRAXAS
BRCC36
ABRO1
BRCC36
F
t(min)
0
5
10
20
30
60
120
180
240
300
360
420
(Ub)2
(Ub)3
(Ub)4
(Ub)3
(Ub)2
Ub
G
v0 (RF/s), IQF (Ub)2
400
200
0
0
200
400
600
BRCA1-A (nM)
H
Kd = 700 ± 200 μM
intensity of Ubiquitin peak
0.07
0.06
0.05
0.04
0.03
0.02
0.01
0
400
800
1200
MERIT40 (μM)
Kd = 20 ± 20 μM
intensity of Ubiquitin peak
0.08
0.06
0.04
0.02
0
-0.02
0
100
200
300
MERIT40-BRE (μM)

Figure S3. Assembly of BRCA1-A and BRISC and functional aspects. Related to Figures 1 and 2

(A) Cartoon representation of mouse BRCC36 (cyan, top left panel) active site. Residues His122, His124, and Asp135, which coordinate the active site zinc atom, and activation residue Glu33, which coordinates water in the active enzyme are highlighted. Asp88, which lies on Ins-1 adjacent to the active site, is shown. The structure of the mouse BRCC36 active site in context of the assembled complex is highly similar to the structure of ant BRCC36 in the BRCC36-KIAA0157 super-dimer (green, top center panel). Comparison to human AMSH-LP (purple, bottom left panel) shows a highly similar active site. The acidic residue Asp321 on the Ins-1 loop of AMSH-LP, which occludes access to the active site, is conserved between BRCC36 and AMSH-LP, and relocates outward upon di-ubiquitin binding (bottom center panel), suggesting a similar mechanism for BRCC36. Close-up of the BRCC36 active site in BRCA1-A showing the protein in cartoon mode (cyan) with side chains shown as sticks and active site residues labelled overlayed with an anomalous log-likelihood gain map segment showing the prominent peak for the Zn^{2+} ion (gray sphere) calculated with *REFMAC* from an intermediate data set and incomplete model is shown mesh (magenta) and contoured at 7.5 rms (top right panel). The same view as above with a segment of final $2mF_o$-DF_c map calculated by *REFMAC* with regularized negative B-factor sharpening (-160 $Å^2$) shown as mesh (blue) at a contour level of 1 rms and displayed at a radius of 15 Å about the Zn^{2+} ion (bottom right panel).

(B) Interaction between the MPN domain of the active protease and the activating MPN scaffold domain are conserved between the ancestral complex containing KIAA0157 and BRCA1-A containing ABRAXAS (and BRISC; not shown). The arrangement in BRCA1-A differs from what is observed in the 19S proteasome lid and CSN complex. Activation of BRCC36 in BRCA1-A is effected by the interaction between Asn170 of the scaffold subunit ABRAXAS with Glu30 of the activation loop of BRCC36 (residues shown as red spheres). This mechanism is found in the ancestral complex and conserved in BRISC, but sterically not possible in CSN and the proteasome lid.

(C) Structural comparison between the structures of the three UBC fold domains of BRE with the active E2 enzyme, an inactive UBC domain, an RWD domain, and the UEV and RWD domains of human FANCL suggest that the central domain of BRE adopts an RWD fold characterized by a long β-sheet 4 directly followed by an α-helical element.

(D) Alignment of human FANCL and BRE shows that the angle between the UEV and RWD domains of FANCL is similar to the extended conformation observed in the BRE RWD and UEV-C domain.

(E) The position of the linker that connects the MPN domain of the scaffold subunit to the long, C-terminal helix II mediating dimerization differs between the ancestral KIAA0157/BRCC36 complex and the mammalian BRCA1-A and BRISC complexes. A schematic depiction follows the linker from the MPN domain to helix II. Unlike in the ancestral complex where the KIAA0157 (green) linker is positioned along the outer surface of the MPN domain, the ABRAXAS (red) linker crosses on top of the helical bundle and effectively cross-links the super-dimer in the mammalian BRCA1-A complex. In BRISC the ABRO1 (yellow) linker takes a path identical to what is observed in BRCA1-A.

(F) BRISC complex processes $(Ub)_4$ faster than $(Ub)_3$ and $(Ub)_2$. K63-linked ubiquitin substrate (150ng/lane) is incubated with 5 nM BRISC on ice and analyzed by silver stained SDS-PAGE. Under these conditions, $(Ub)_4$ is cleaved within 5 minutes, while $(Ub)_2$ and $(Ub)_3$ are not cleaved within 7 hours.

(G) BRCA1-A is able to efficiently cleave di-Ubiquitin at higher temperature and enzyme concentration. Enzyme titration of BRCA1-A degrading 200 nM internally quenched K63-linked di-Ubiquitin shows increasing v_0 (in relative fluorescence units per second) with increasing enzyme concentration. Error bars represent mean ± SD of n = 3 replicates. Since no saturation was observed using practical concentrations of fluorescent substrate, we were not able to determine the kinetic parameters.

(H) MERIT40 and the MERIT40-BRE complex bind ubiquitin. NMR binding assay by titration of MERIT40 or MERIT40-BRE into ^{15}N-labeled ubiquitin. Peak intensity for ten representative peaks in the HSQC spectrum were measured and plotted as a function of MERIT40 concentration in the titration. Peak intensity diminished as the peaks broadened from the larger molecular weight complex that is formed and/or intermediate exchange. Data were fit to a one-site binding model assuming the bound state has zero peak intensity. The reported K_d is the average affinity over tracking the ten peaks with the standard deviation reported as error.

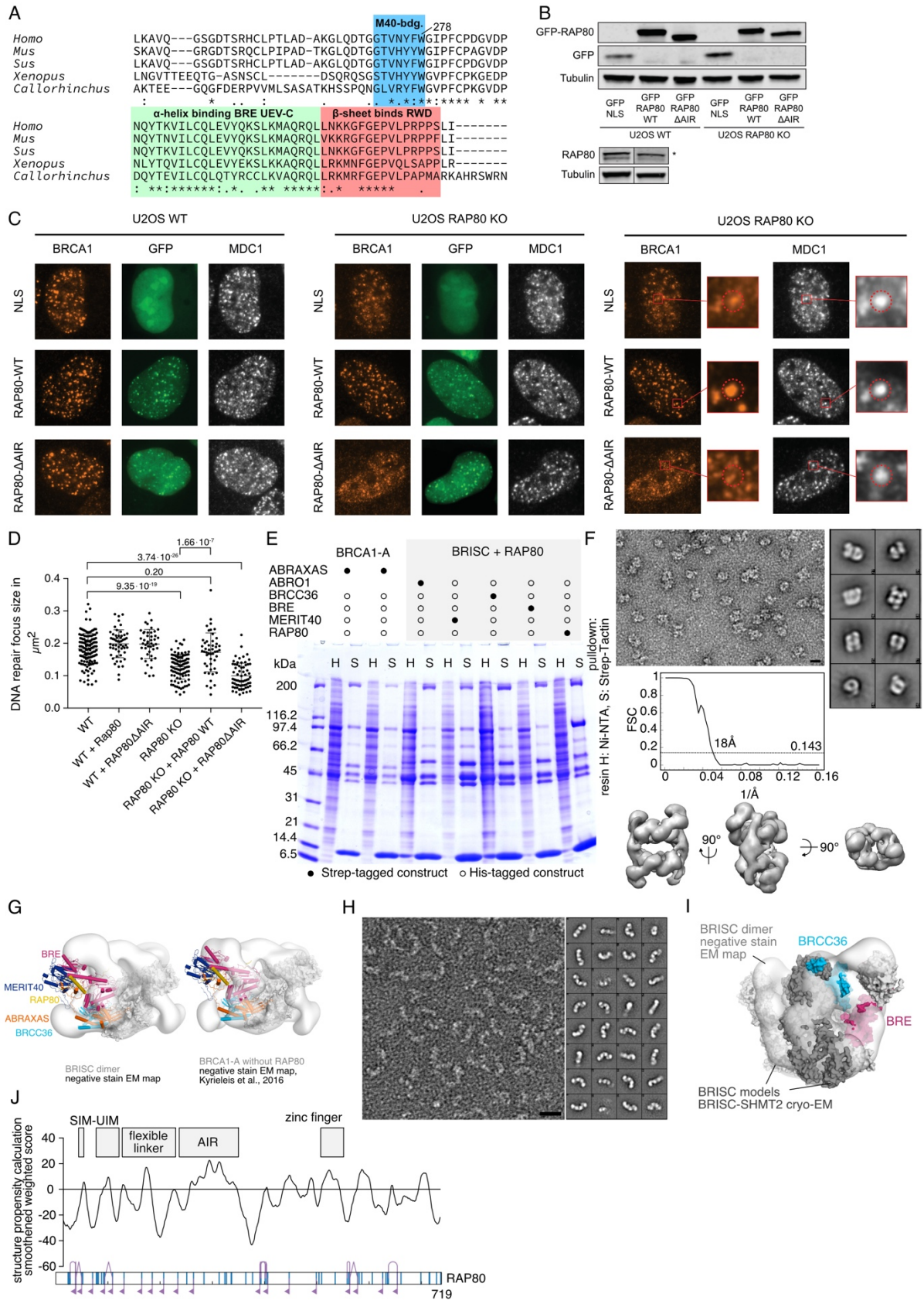
A
M40-bdg.
278
Homo LKAVQ---GSGDTSRHCLPTLAD-AKGLQDTGGTVNYFWGIPFCPDGVDP
Mus SKAVQ---GRGDTSRQCLPIPAD-TKGLQDTGGTVHYYWGIPFCPAGVDP
Sus LKAVQ---GSGDTSRHCLPTLAD-AKGLQDTGGTVNYFWGIPFCPDGVDP
Xenopus LNGVTTEEQTG-ASNSCL-------DSQRQSGSTVHYYWGVPFCPKGEDP
Callorhinchus AKTEE---GQGFDERPVVMLSASATKHSSPQNGLVRYFWGVPFCPKGVDP
α-helix binding BRE UEV-C
β-sheet binds RWD
Homo NQYTKVILCQLEVYQKSLKMAQRQLLNKKGFGEPVLPRPPSLI-------
Mus NQYTNVILCQLEVYQKSLKMAQRQLVKKRGFGEPVLPRPPFLI-------
Sus NQYTKVILCQLEVYQKSLKMAQRQLLNKKGFGEPVLPRPPSLI-------
Xenopus NLYTQVILCQLEVYEKSLKKAQRQLLRKMNFGEPVQLSAPPLR-------
Callorhinchus DQYTEVILCQLQTYRCCLKVAQRQLLRKMRFGEPVLPAPMARKAHRSWRN
B
GFP-RAP80
GFP
Tubulin
GFP NLS
GFP RAP80 WT
GFP RAP80 ΔAIR
GFP NLS
GFP RAP80 WT
GFP RAP80 ΔAIR
U2OS WT
U2OS RAP80 KO
RAP80
Tubulin
C
U2OS WT
U2OS RAP80 KO
U2OS RAP80 KO
BRCA1
GFP
MDC1
NLS
RAP80-WT
RAP80-ΔAIR
D
DNA repair focus size in μm²
1.66·10⁻⁷
3.74·10⁻²⁶
0.20
9.35·10⁻¹⁹
WT
WT + Rap80
WT + RAP80ΔAIR
RAP80 KO
RAP80 KO + RAP80 WT
RAP80 KO + RAP80ΔAIR
E
BRCA1-A
BRISC + RAP80
ABRAXAS
ABRO1
BRCC36
BRE
MERIT40
RAP80
kDa
H S H S H S H S H S H S H S
200
116.2
97.4
66.2
45
31
21
14.4
6.5
Strep-tagged construct
His-tagged construct
F
pulldown: resin H: Ni-NTA, S: Strep-Tactin
FSC
18Å
0.143
1/Å
90°
90°
G
BRE
MERIT40
RAP80
ABRAXAS
BRCC36
BRISC dimer negative stain EM map
BRCA1-A without RAP80 negative stain EM map, Kyrieleis et al., 2016
H
I
BRISC dimer negative stain EM map
BRCC36
BRE
BRISC models BRISC-SHMT2 cryo-EM
J
SIM-UIM
flexible linker
AIR
zinc finger
structure propensity calculation smoothened weighted score
RAP80
719

Figure S4. Functionalization of BRCA1-A by RAP80 and ABRAXAS, Related to Figures 2 and 3

(A) Alignment of RAP80 from human, mouse, pig, frog, and chimaera, shows highly conserved AIR domains. The label for the conserved tryptophan residue refers to the position in the human/mouse protein.

(B) Expression of GFP-fusion RAP80 constructs (star denotes unspecific band) was controlled by western blotting with an antibody against GFP.

(C) The minimal ABRAXAS binding region observed in the structure is essential for RAP80 binding to ubiquitin in vivo. Wild-type and RAP80 knockout U2OS cells were transfected with either GFP-NLS, GFP-RAP80 or GFP-RAP80ΔAIR. Cells were irradiated and focus formation was monitored by staining for MDC1 and BRCA1. The right panel shows the BRCA1 stained cells of the central panel with individual foci enlarged for comparison. BRCA1 foci were formed in wild-type cells as well as in KO cells transfected with wild-type RAP80. RAP80 devoid of the AIR domain forms RAP80 foci comparable to wild-type RAP80 but was unable to rescue BRCA1 focus formation, giving rise to fewer and smaller BRCA1 foci.

(D) Quantification shows a reduction of BRCA1 focus size by almost 50% in RAP80 KO cells that cannot be rescued by transfection with GFP-RAP80ΔAIR. Error bars represent mean ± SD. Number of replicates: WT n = 134, WT + RAP80 n = 56, WT + RAP80ΔAIR n = 45, RAP80 KO n = 107, RAP80 KO + RAP80 WT n = 50, RAP80 KO + RAP80ΔAIR n = 71.

(E) Co-expression of tagged subunits in insect cells was used to assess integration of RAP80 into BRCA1-A and BRISC. BRCA1-A integrates RAP80 stoichiometrically when co-expressed in insect cells, as shown for two independently generated sets of baculoviruses encoding BRCA1-A subunits. Co-expression of RAP80 with BRISC subunits on the other hand does not result in stoichiometric integration of RAP80 into the complex.

(F) The structure of BRISC was determined by 3D reconstruction from negative stain electron micrographs. Negative stain electron micrographs (scale bar: 150 Å), class averages, the FSC curve (18Å at FSC = 0.143) and a three-dimensional reconstruction are shown.

(G) Rigid body fitting of the BRCA1-A crystal structure into the BRISC dimer map (left) and the truncated RAP80-less BRCA1-A (Kyrieleis et al., 2016) map (right) shows that BRE and MERIT40 adopt a different conformation in fully assembled BRCA1-A with integrated RAP80 than in the two RAP80-less complexes.

(H) Negative stain electron micrograph (scale bar: 150 Å) and class averages of GraFix crosslinked BRCA1-A shows the single arc conformation only.

(I) Dimerization of BRISC is effected by an interaction between BRCC36 and BRE.

(J) Aside from the AIR domain embedded into BRCA1-A complex, RAP80 is largely flexible and unstructured as evidenced by structure prediction analysis of RAP80 sequence and by prevalence of monolinks in crosslinking-MS experiments of BRCA1-A complex.

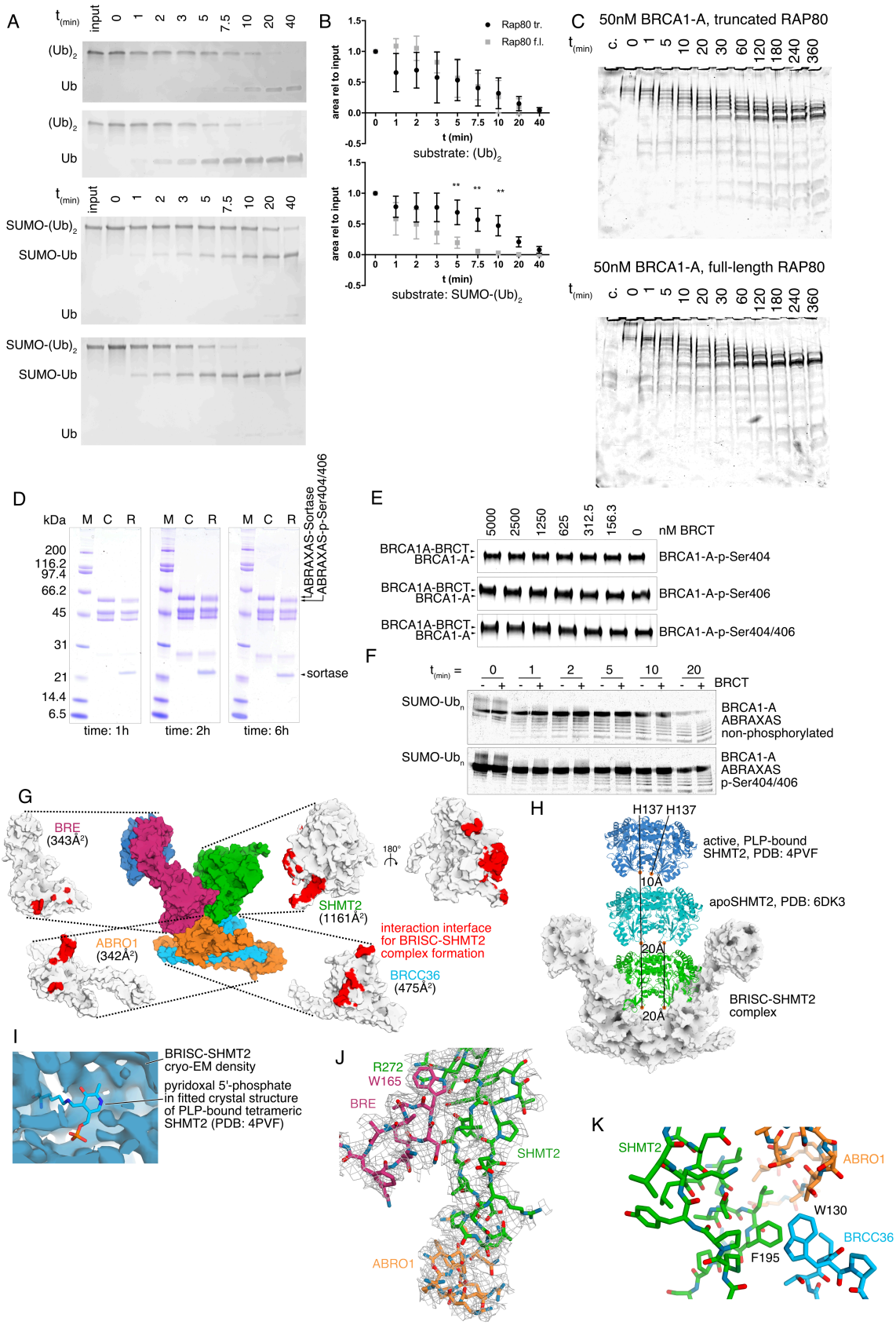
A
t(min) input 0 1 2 3 5 7.5 10 20 40
(Ub)2
Ub
SUMO-(Ub)2
SUMO-Ub
B
Rap80 tr.
Rap80 f.l.
area rel to input
t (min)
substrate: (Ub)2
substrate: SUMO-(Ub)2
C
50nM BRCA1-A, truncated RAP80
50nM BRCA1-A, full-length RAP80
t(min) c. 0 1 5 10 20 30 60 120 180 240 360
D
kDa M C R
200
116.2
97.4
66.2
45
31
21
14.4
6.5
ABRAXAS-Sortase
ABRAXAS-p-Ser404/406
sortase
time: 1h
time: 2h
time: 6h
E
5000 2500 1250 625 312.5 156.3 0 nM BRCT
BRCA1A-BRCT-BRCA1-A
BRCA1-A-p-Ser404
BRCA1-A-p-Ser406
BRCA1-A-p-Ser404/406
F
t(min) = 0 1 2 5 10 20
BRCT
SUMO-Ubn
BRCA1-A ABRAXAS non-phosphorylated
BRCA1-A ABRAXAS p-Ser404/406
G
BRE (343Å2)
ABRO1 (342Å2)
SHMT2 (1161Å2)
BRCC36 (475Å2)
180°
interaction interface for BRISC-SHMT2 complex formation
H
H137 H137
active, PLP-bound SHMT2, PDB: 4PVF
10Å
apoSHMT2, PDB: 6DK3
20Å
20Å
BRISC-SHMT2 complex
I
BRISC-SHMT2 cryo-EM density
pyridoxal 5'-phosphate in fitted crystal structure of PLP-bound tetrameric SHMT2 (PDB: 4PVF)
J
R272
W165
BRE
SHMT2
ABRO1
K
SHMT2
ABRO1
W130
BRCC36
F195

Figure S5. BRCA1-A DUB activity, BRCA1 sequestration and BRISC-SHMT2α interactions. Related to Figure 3, 4, and 5.

(A) Specificity of BRCA1-A in degrading Ubiquitin and mixed chains was assessed using BRCA1-A with full-length or truncated RAP80 and di-Ubiquitin or SUMO-di-Ubiquitin as substrates. Deubiquitination reactions were sampled, analyzed and quantified by SYPRO Ruby staining.

(B) BRCA1-A with full-length RAP80 degrades SUMO-di-Ubiquitin faster compared to BRCA1-A complex with truncated RAP80. Degradation speed of $(Ub)_2$ is independent of the presence of the RAP80 SIM-UIM_2 domains. Error bars represent mean ± SD of n = 3 replicates.

(C) Long K63-linked $(SUMO)_4$-$(Ub)_n$ chains are rapidly degraded by BRCA1-A irrespective of the presence or absence of the RAP80 SIM-UIM_2 domains.

(D) Progress of the sortase labeling reaction of engineered BRCA1-A with phosphorylated C-terminal ABRAXAS peptides is shown by band shift in SDS-PAGE.

(E) BRCA1-BRCT binds BRCA1-A when ABRAXAS is phosphorylated either p-Ser404 or p-Ser404/406, but does not form larger aggregates, as evidenced by shift on native PAGE.

(F) Binding of BRCA1-BRCT does not attenuate DUB activity against long mixed SUMO-Ubiquitin chains. Timed deubiquitination reactions were analyzed by SDS-PAGE and silver stain.

(G) SHMT2α binds to three subunits of BRISC: BRE, ABRO1 and BRCC36. Subunits are shown in white with the interaction surfaces shown in red.

(H) The SHMT2α dimer binds BRISC in a conformation similar to the inactive, apoSHMT2α, where the distance between His137 of the respective protomers is ~20 Å, instead of the conformation in the active, PLP-bound SHMT2α, where His137 of both protomers are more proximal at ~10 Å distance.

(I) PLP is absent in the BRISC-SHMT2α complex cryo-EM density.

(J) The SHMT2α BRISC-binding loop is extending towards BRE and ABRO1. Interactions between Arg272 of SHMT2α and Trp165 of BRE and between Arg153 and Tyr154 of ABRO1 and Asp279 and Pro280 of SHMT2α are observed.

(K) SHMT2α interacts with BRCC36: Phe195 of SHMT2α binds Trp130 of BRCC36.

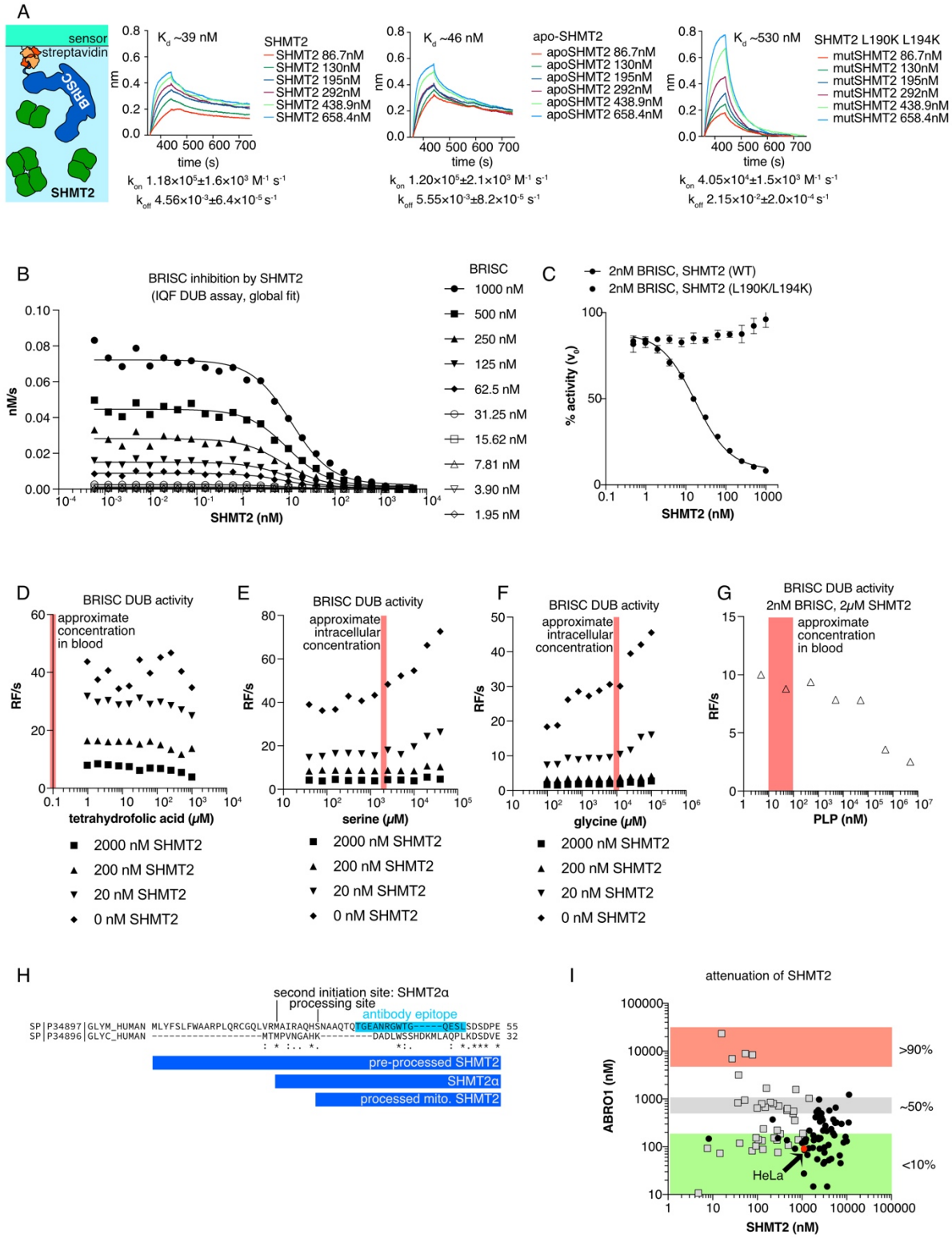
A
sensor
streptavidin
BRISC
SHMT2
K_d ~39 nM
SHMT2
SHMT2 86.7nM
SHMT2 130nM
SHMT2 195nM
SHMT2 292nM
SHMT2 438.9nM
SHMT2 658.4nM
nm
time (s)
k_on 1.18×10^5±1.6×10^3 M^-1 s^-1
k_off 4.56×10^-3±6.4×10^-5 s^-1
K_d ~46 nM
apo-SHMT2
apoSHMT2 86.7nM
apoSHMT2 130nM
apoSHMT2 195nM
apoSHMT2 292nM
apoSHMT2 438.9nM
apoSHMT2 658.4nM
k_on 1.20×10^5±2.1×10^3 M^-1 s^-1
k_off 5.55×10^-3±8.2×10^-5 s^-1
K_d ~530 nM
SHMT2 L190K L194K
mutSHMT2 86.7nM
mutSHMT2 130nM
mutSHMT2 195nM
mutSHMT2 292nM
mutSHMT2 438.9nM
mutSHMT2 658.4nM
k_on 4.05×10^4±1.5×10^3 M^-1 s^-1
k_off 2.15×10^-2±2.0×10^-4 s^-1
B
BRISC inhibition by SHMT2
(IQF DUB assay, global fit)
nM/s
SHMT2 (nM)
BRISC
1000 nM
500 nM
250 nM
125 nM
62.5 nM
31.25 nM
15.62 nM
7.81 nM
3.90 nM
1.95 nM
C
2nM BRISC, SHMT2 (WT)
2nM BRISC, SHMT2 (L190K/L194K)
% activity (v_0)
SHMT2 (nM)
D
BRISC DUB activity
approximate concentration in blood
RF/s
tetrahydrofolic acid (μM)
2000 nM SHMT2
200 nM SHMT2
20 nM SHMT2
0 nM SHMT2
E
BRISC DUB activity
approximate intracellular concentration
RF/s
serine (μM)
2000 nM SHMT2
200 nM SHMT2
20 nM SHMT2
0 nM SHMT2
F
BRISC DUB activity
approximate intracellular concentration
RF/s
glycine (μM)
2000 nM SHMT2
200 nM SHMT2
20 nM SHMT2
0 nM SHMT2
G
BRISC DUB activity
2nM BRISC, 2μM SHMT2
approximate concentration in blood
RF/s
PLP (nM)
H
second initiation site: SHMT2α
processing site
antibody epitope
SP|P34897|GLYM_HUMAN MLYFSLFWAARPLQRCGQLVRMAIRAQHSNAAQTQTGEANRGWTG-----QESLSDSDPE 55
SP|P34896|GLYC_HUMAN ----------MTMPVNGAHK---------DADLWSSHDKMLAQPLKDSDVE 32
pre-processed SHMT2
SHMT2α
processed mito. SHMT2
I
attenuation of SHMT2
ABRO1 (nM)
SHMT2 (nM)
>90%
~50%
<10%
HeLa

Figure S6. SHMT2α is an inhibitor of BRISC, related to Figures 5, 6 and 7

(A) SHMT2α binds BRISC with nanomolar affinity in a biolayer interferometry (BIF) experiment. Raw kinetic traces are shown, phase shift (nm) vs time (s); k_{on} and k_{off} were determined by global fit. SHMT2α lacking the PLP cofactor (apoSHMT2) binds with the same affinity as PLP-preincubated SHMT2α to BRISC in BIF. Raw kinetic traces are shown; k_{on} and k_{off} were determined by global fit. Mutation of Leu190 and Leu194 of SHMT2α to lysine increases k_{on} and k_{off}, reducing the affinity of SHMT2α for BRISC by an order of magnitude in BIF. Raw kinetic traces are shown; k_{on} and k_{off} were determined by global fit.

(B) SHMT2α inhibits BRISC with nanomolar K_i in an internally quenched fluorescent (IQF) di-ubiquitin assay. The reaction was set up in dilution replicates (n = 10) and K_i was determined by global fit.

(C) The Leu190Lys Leu194Lys SHMT2α mutant, which binds with far lower affinity than the wild type does not inhibit BRISC in the IQF DUB assay. Error bars represent mean ± SD of n = 3 replicates.

(D) Tetrahydrofolic acid does not affect activity of BRISC or inhibition by SHMT2α in the IQF DUB assay at concentrations around and above those found in human blood (Wishart et al., 2017).

(E) Serine does not affect activity of BRISC or inhibition by SHMT2α in the IQF DUB assay at concentrations around and above those found inside human cells (Chaneton et al., 2012).

(F) Glycine does not affect activity of BRISC or inhibition by SHMT2α in the IQF DUB assay at concentrations around and above those found inside human cells (Chaneton et al., 2012).

(G) Pyridoxal 5'-phosphate does not affect activity of BRISC or inhibition by SHMT2α in the IQF DUB assay at concentrations around and above those found in human blood (Wishart et al., 2017).

(H) Schematic representation of SHMT2 N-terminus processing. The SHMT2 gene gives rise to three isoforms of the enzyme: pre-processed SHMT2, SHMT2α and processed, mitochondrial SHMT2.

(I) Estimated concentrations of ABRO1 and SHMT2 for human tissues (gray rectangles) and cell lines (black circles). Estimated regions of low (green), medium (grey) and high attenuation (red) of SHMT2 function are shown. HeLa cells are shown in red. This figure assumes that inhibition kinetics of SHMT2 by BRISC is analogous to BRISC inhibition by SHMT2.

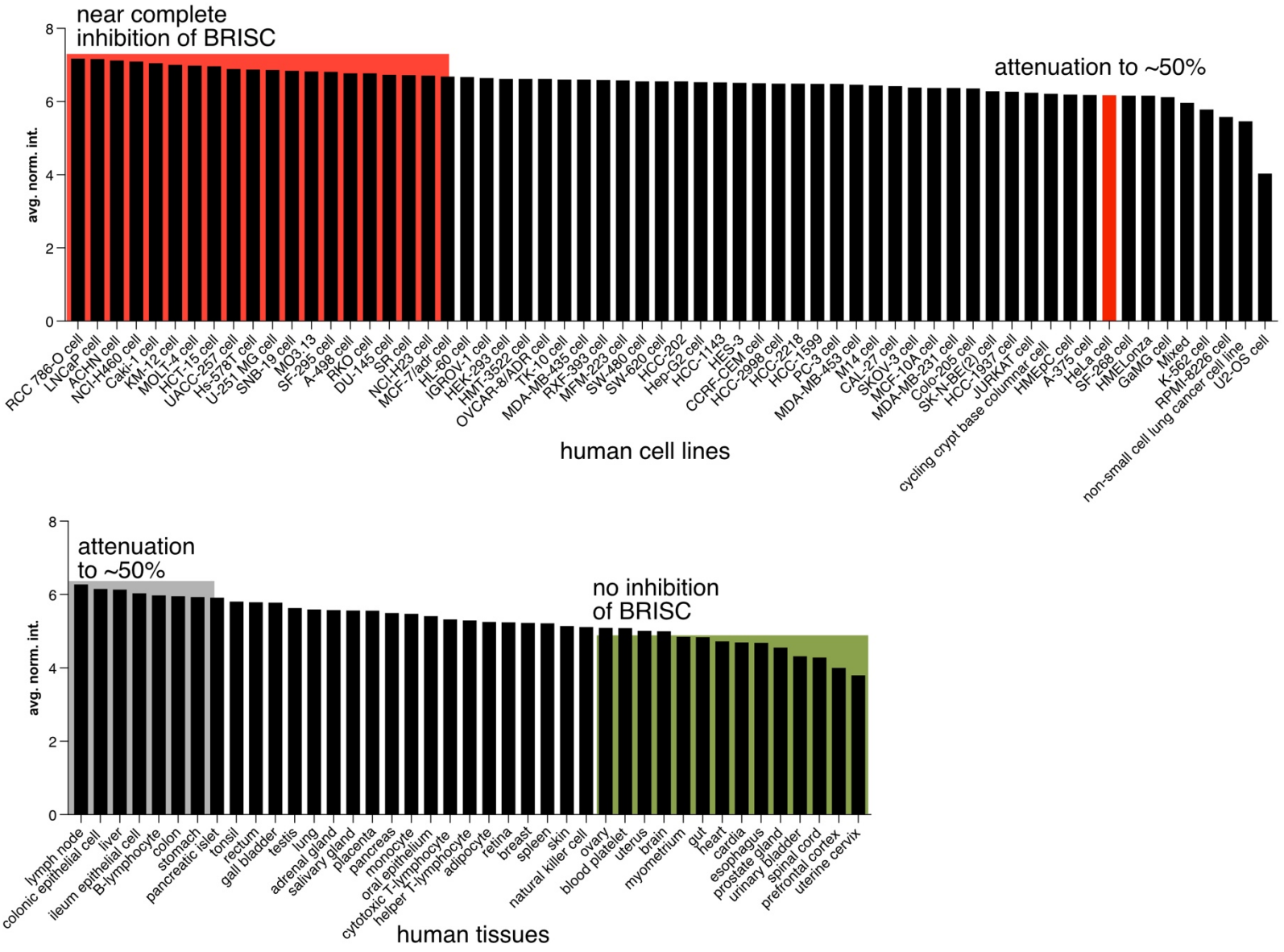
near complete
inhibition of BRISC
attenuation to ~50%
avg. norm. int.
0
2
4
6
8
RCC 786-O cell
LNCaP cell
ACHN cell
NCI-H460 cell
Caki-1 cell
KM-12 cell
MOLT-4 cell
HCT-15 cell
UACC-257 cell
Hs-578T cell
U-251 MG cell
SNB-19 cell
MO3.13
SF-295 cell
A-498 cell
RKO cell
DU-145 cell
SR cell
NCI-H23 cell
MCF-7/adr cell
HL-60 cell
IGROV-1 cell
HEK-293 cell
HMT-3522 cell
OVCAR-8/ADR cell
TK-10 cell
MDA-MB-435 cell
RXF-393 cell
MFM-223 cell
SW-480 cell
SW-620 cell
HCC-202
Hep-G2 cell
HCC-1143
HES-3
CCRF-CEM cell
HCC-2998 cell
HCC-2218
HCC-1599
PC-3 cell
MDA-MB-453 cell
M14 cell
CAL-27 cell
SKOV-3 cell
MCF-10A cell
MDA-MB-231 cell
Colo-205 cell
SK-N-BE(2) cell
HCC-1937 cell
JURKAT cell
cycling crypt base columnar cell
HMEpC cell
A-375 cell
HeLa cell
SF-268 cell
HMELonza
GaMG cell
Mixed
K-562 cell
RPMI-8226 cell
non-small cell lung cancer cell line
U2-OS cell
human cell lines
attenuation
to ~50%
no inhibition
of BRISC
avg. norm. int.
0
2
4
6
8
lymph node
colonic epithelial cell
liver
ileum epithelial cell
B-lymphocyte
colon
stomach
pancreatic islet
tonsil
rectum
gall bladder
testis
lung
adrenal gland
salivary gland
placenta
pancreas
monocyte
oral epithelium
cytotoxic T-lymphocyte
helper T-lymphocyte
adipocyte
retina
breast
spleen
skin
natural killer cell
ovary
blood platelet
uterus
brain
myometrium
gut
heart
cardia
esophagus
prostate gland
urinary bladder
spinal cord
prefrontal cortex
uterine cervix
human tissues

Figure S7. SHMT2 reaches inhibitory concentrations in cancer cells, Related to Figure 6 The average normalized intensity for SHMT2 in the quantitative mass-spectroscopic study of Wilhelm et al., 2014 is shown for human tissues and human cell lines. The absolute concentration of SHMT2 in HeLa cells determined by Hein et al., 2015 (red bar) was used to infer the approximate absolute concentrations of SHMT2 in the other tissues and cell lines. At SHMT2 concentrations around 1 μM and concentrations of BRISC around 50 nM, as found in HeLa cells, BRISC DUB activity is reduced by 50%. Most human tissues have lower concentrations of SHMT2, suggesting that BRISC action is attenuated in some tissues (gray), but not others (green). Cancer cell lines have far higher concentrations of SHMT2 than human tissues: most cancer cell lines surveyed contain higher concentrations of SHMT2 than HeLa, suggesting that BRISC DUB activity is nearly completely inhibited (red) in most cancer cell lines.